

# Nanoscale

Accepted Manuscript



This is an *Accepted Manuscript*, which has been through the Royal Society of Chemistry peer review process and has been accepted for publication.

*Accepted Manuscripts* are published online shortly after acceptance, before technical editing, formatting and proof reading. Using this free service, authors can make their results available to the community, in citable form, before we publish the edited article. We will replace this *Accepted Manuscript* with the edited and formatted *Advance Article* as soon as it is available.

You can find more information about *Accepted Manuscripts* in the [Information for Authors](#).

Please note that technical editing may introduce minor changes to the text and/or graphics, which may alter content. The journal's standard [Terms & Conditions](#) and the [Ethical guidelines](#) still apply. In no event shall the Royal Society of Chemistry be held responsible for any errors or omissions in this *Accepted Manuscript* or any consequences arising from the use of any information it contains.

# Surface Functionalized Nanopore Titania Integrated Microfluidic Biochip

Md. Azahar Ali<sup>1,2</sup>, Saurabh Srivastava<sup>1</sup>, Kunal Mondal<sup>3</sup>, Pandurang M. Chavhan<sup>1</sup>, Ved V. Agrawal<sup>1\*</sup>, Renu John<sup>2\*</sup>, Ashutosh Sharma<sup>3\*</sup>, Bansi D. Malhotra<sup>1,4\*</sup>

<sup>1</sup>Department of Science and Technology Centre on Biomolecular Electronics, Biomedical Instrumentation Section, CSIR-National Physical Laboratory, Dr. K. S. Krishnan Marg, New Delhi-110012, India

<sup>2</sup>Biomedical Engineering, Indian Institute of Technology Hyderabad, Ordnance Factory Estate, Yeddumailaram, Hyderabad, AP, 502205, India

<sup>3</sup>Department of Chemical Engineering, Indian Institute of Technology Kanpur, Kanpur-208016, India

<sup>4</sup>Department of Biotechnology, Delhi Technological University, Shahbad, Daulatpur, Main Bawana Road, Delhi-110042, India

## Abstract

We demonstrate a novel and an efficient nanopore microfluidic biochip consisting of a functionalized chitosan/anatase titanium dioxide nanoparticles (antTiO<sub>2</sub>-CH) electrode integrated in a polymethylsiloxane (PDMS) microchannel assembly. The electrode surface can be enzyme functionalized depending on the application. We study in detail cholesterol sensing using the cholesterol esterase (ChEt) and cholesterol oxidase (ChOx) functionalized chitosan supported mesoporous antTiO<sub>2</sub>-CH microfluidic electrode. The available functional groups present in nanoporous antTiO<sub>2</sub>-CH surface in this microfluidic biochip can play an important role for enzyme functionalization, which has been quantified by X-ray photoelectron spectroscopic technique. The Brunauer-Emmett-Teller (BET) studies are used to quantify the specific surface area and nanopore size distribution of titania nanoparticles with and without chitosan. Point defects in antTiO<sub>2</sub> can increase the heterogeneous electron transfer constant between electrode and enzyme active sites resulting in improved electrochemical behaviour of the microfluidic biochip. The impedimetric response of the nanopore microfluidic biochip (ChEt-ChOx/antTiO<sub>2</sub>-CH) shows high sensitivity of 6.77 kΩ/mgdl<sup>-1</sup> in the range of 2-500 mg/dl, a low detection limit of 0.2 mg/dl, a low Michaelis–Menten constant of 1.3 mg/dl and a high selectivity. This impedimetric microsystem has enormous potential for clinical diagnostics applications.

**Keywords:** Nanopore, anatase-TiO<sub>2</sub>, Microfluidic electrode, Polydimethylsiloxane, Photolithography, Impedance spectroscopy, Biomolecules detection

---

\*Corresponding Authors: [bansi.malhotra@gmail.com](mailto:bansi.malhotra@gmail.com); Phone: +91-011-45609152, Fax: +91-011-45609310, [renujohn@iith.ac.in](mailto:renujohn@iith.ac.in), [ved.varun@gmail.com](mailto:ved.varun@gmail.com) and [ashutos@iitk.ac.in](mailto:ashutos@iitk.ac.in)

## Introduction

Microfabrication techniques along with electrochemical methods have recently received considerable attention for detection of desired biomolecules in clinical diagnostics.<sup>1,2</sup> The impedance spectroscopy is the study of resistive and capacitive behavior of an electrode–electrolyte interface in a given frequency domain.<sup>1-4</sup> The impedimetric method is known to be a non-destructive, sensitive and label-free analytical detection technique that can be utilized to investigate a bio-recognition event occurring at an electrode/electrolyte interface.<sup>4</sup> Besides this, EIS can be used to obtain information on biomolecular interactions, amount of adsorbed proteins, surface charge densities and the magnitude of adsorption coefficient.<sup>5</sup> The electrochemical impedance spectroscopy (EIS) uses a small perturbation (usually sinusoidal) which reduces the matrix interference and rapidly responds to the change caused due to binding of an analyte with immobilized bio-recognition element on the transducer surface.<sup>1-5</sup> An impedimetric cholesterol sensor based on Fe<sub>3</sub>O<sub>4</sub> nanoparticles with a sensitivity of 6 Ω/mg dl<sup>-1</sup>/cm<sup>2</sup> and a detection time of 25 s has recently been reported.<sup>6</sup> However, the use of impedimetric macro-electrodes may perhaps lead to poor sensitivity, detection time and limit. Besides this, a miniaturized microfluidic biochip or a Lab-on-a chip (LOC)-based biosensing device has many advantages such as the use of reduced volumes and chemical reagents, precise control of fluids, low cost and thus provide versatile format for integration of the various detection platforms.<sup>7-15</sup> As an example, Arya *et al.* have recently demonstrated a microelectrode-based EIS sensor that provides rapid reaction kinetics, improved sensitivity, large electrode aspect ratio and increased signal-to-noise ratio.<sup>16</sup>

Many researchers have utilized nanostructured metal oxides for fabrication of microfluidic biosensors.<sup>17</sup> Nanostructured titania (TiO<sub>2</sub>) is an exciting transducer material for fabrication of miniaturized biosensors because of its large surface-to-volume ratio and relatively short diffusion length properties.<sup>18-20</sup> The application of TiO<sub>2</sub> in photocatalysis<sup>21</sup>, solar cells<sup>22</sup>, rechargeable lithium batteries<sup>23</sup> and biosensors<sup>24</sup> has recently been explored. Wang *et al.* demonstrated a TiO<sub>2</sub> nanowire bundle microelectrode-based impedance immunosensor for rapid and sensitive detection of *Listeria monocytogenes*.<sup>25</sup> It has been found that nanostructured TiO<sub>2</sub> is a multifunctional material due to its long-term chemical stability, large specific surface area, negligible protein denaturation and good biocompatibility.<sup>26</sup> The high percentage of reactive (001) facets of anatase TiO<sub>2</sub> nanocrystal (tetragonal, space group *I4<sub>1</sub>/amd*) can be used to obtain

enhanced catalytic activity, improved stability and selectivity.<sup>27,28</sup> Oxygen vacancies on TiO<sub>2</sub> surface (110) may perhaps govern the surface chemistry because of their potential to stabilize the binding of surface species.<sup>29</sup> The point defects in TiO<sub>2</sub> arising due to oxygen vacancy sites are perhaps located within the bridging oxygen rows of the TiO<sub>2</sub>(110)–(1×1) surface.<sup>30</sup> The presence of Ti<sup>3+</sup> defects may lead to improved adsorption of enzyme molecules and fast heterogeneous electron transfer rate of TiO<sub>2</sub> resulting in enhanced sensitivity and improved response time of a microfluidic sensor.<sup>29</sup> Ali. *et al.* reported that antTiO<sub>2</sub> nanoparticles can be used to electrochemically activate the enzyme due to presence of gibbositities on the antTiO<sub>2</sub> surface resulting in decreased tunneling distance between active site of enzyme and electrode leading to enhanced electrochemical current.<sup>26</sup> However, the direct attachment of biomolecules onto antTiO<sub>2</sub> surface continues to be a major limitation as its surface can absorb only a limited number of desired biomolecules due to weak inter-molecular interactions with the biomolecules. We explore overcoming this limitation by using a nanocomposite material comprising of a biopolymer (e. g. chitosan) and antTiO<sub>2</sub> nanoparticles since chitosan could act as a template for dispersion of antTiO<sub>2</sub> nanoparticles, thereby facilitating improved enzyme functionalization.

The chitosan (CH), a deacetylation product of chitin, is a functional and basic polysaccharide composed of β-1,4-linked glucosamine that can be extracted from the exoskeletons of shrimps and crabs.<sup>31</sup> This interesting biomaterial offers excellent film forming ability and acts as a stabilizing agent. It is also cost-effective, biocompatible and biodegradable. The porous structure of CH can be used to obtain enhanced dispersion of TiO<sub>2</sub> nanoparticles that may provide sufficient electron-conducting paths and high surface area for adsorption of biomolecules such as enzymes, proteins etc. Crossland *et al.* reported an optoelectronic device using mesoporous anatase TiO<sub>2</sub> single crystal.<sup>32</sup> This synthesized nanopore TiO<sub>2</sub> shows excellent conductivity and electron mobility compared to that of conventional nanocrystalline TiO<sub>2</sub>.<sup>32</sup> The nanoporosity of TiO<sub>2</sub> may result in highly accessible surfaces leading to improved biosensor characteristics. Wagner *et al.* have observed improved performance of mesoporous materials based gas sensors.<sup>33</sup> A nanopore TiO<sub>2</sub> biosensor may also result in higher diffusion coefficient compared to that of non-ordered silica material.<sup>34</sup> The nanopore structure of titania may promote both CH and biomolecules adsorption resulting in improved electron diffusivity. The high porosity and excellent surface area of titania could thus provide a favorable platform for incorporation of CH resulting in higher biomolecules loading. In addition, the available

functional groups such as the amino (-NH<sub>2</sub>), hydroxyl (-OH) *etc.* of CH offer a hydrophilic environment for a given biomolecule. Feng *et al.* have developed a porous metal oxide-CH matrix for immobilization of single stranded DNA probe for detection of a cancer gene.<sup>31</sup> The nanopore antTiO<sub>2</sub>-CH may perhaps provide a faster electron transfer rate resulting in improved electrochemical properties. The semiconducting nature of anatase TiO<sub>2</sub> nanoparticles in this microfluidic system can enhance the impedance signal i.e. charge transfer resistance implying higher sensitivity. Thus, the nanopore antTiO<sub>2</sub>-CH composite is a new, simple and low cost platform to integrate with microfluidic device for esterified cholesterol monitoring.

In this manuscript, we investigate the surface functionalization of a microfluidic biochip based on nanoporous antTiO<sub>2</sub>-CH composite matrix. This microfluidic biochip consists of nanostructured antTiO<sub>2</sub> grafted CH dip-coated onto an ITO microelectrode and functionalized using bienzyme (cholesterol esterase and cholesterol oxidase). To quantify the functional groups and point defects on nanoporous antTiO<sub>2</sub>-CH surface before and after enzyme functionilzation, we have conducted X-ray photoelectron spectroscopic studies. We use an ac impedance spectroscopic technique for estimation of total cholesterol concentration. The bienzyme functionalized nanoporous antTiO<sub>2</sub>-CH electrode has been characterized using electron microscopy, Brunauer–Emmett–Teller surface area, Fourier transform infra-red/Raman spectroscopy and electrochemical techniques.

## Results and discussions

### Fabrication of Biochip

A detail of fabrication of the nanopore microfluidic biochip has been described in the Methods Section. Figure 1 (i and ii) shows the schematic and a photograph of proposed microfluidic biochip. The thicknesses were measured by an optical profiler in the noncontact mode. Figure 1a shows an optical 3D profiling image of the ITO film coated on a glass in which the thickness has been calculated to be as  $\sim 299 \pm 36$  nm. Then, nanopore antTiO<sub>2</sub>-CH was deposited on the ITO by dip coating method and the thickness was found to be  $\sim 196 \pm 30$  nm. Figure 1b shows the optical 3D profiling image of the antTiO<sub>2</sub>-CH film on ITO. Figure 1c shows 2D atomic force micrograph image (AFM) of antTiO<sub>2</sub> nanoparticles on ITO surface. It can be seen that antTiO<sub>2</sub> nanoparticles are well-aligned, spherical in shape, porous, mono-dispersed and are uniformly distributed on the ITO surface. The average size of the antTiO<sub>2</sub> nanoparticles varies from 10 to

35 nm. The antTiO<sub>2</sub> nanoparticles size distribution is shown in the inset of Figure 1(c). It has been found that average roughness of antTiO<sub>2</sub> film is 0.60 nm.

### Morphological Studies

The surface morphology of the antTiO<sub>2</sub> nanoparticles and chitosan coated/embedded nanoparticles has been explored using field emission-scanning electron microscopy (FE-SEM). The antTiO<sub>2</sub> nanoparticles are dispersed uniformly throughout the ITO surface. It also illustrates that the antTiO<sub>2</sub> nanoparticles are densely distributed. The FE-SEM analysis of titania nanoparticles reveals that the particle size varies from 10 to 35 nm. The average diameter of the TiO<sub>2</sub> particles is estimated to be as ~27 nm. The FE-SEM (Figure 2a) studies reveal porous morphology of the (antTiO<sub>2</sub>-CH) film indicating formation of the antTiO<sub>2</sub>-CH hybrid. This may be attributed to electrostatic interactions between cationic CH and the presence of surface charged antTiO<sub>2</sub> nanoparticles grafted in the CH network (Figure 2b). The micrograph reveals that the hybrid surface (Figure 2b) is coated with the TiO<sub>2</sub> nanoparticles. After enzyme incorporation on antTiO<sub>2</sub>-CH surface (image c), the film morphology is altered. This may be due to three dimensional environment of hybrid surface that promotes coating via formation of complex around apexes and voids and the nanoporous surface structure of antTiO<sub>2</sub>-CH provides increased loading capacity of the bienzyme (ChEt-ChOx).

### Spectroscopic Studies

Figure 3(i) shows XPS wide scan spectrum obtained for the antTiO<sub>2</sub>-CH (a) and ChEt-ChOx/antTiO<sub>2</sub>-CH (b) electrodes on ITO surface. The peaks found at 199.5 eV, 284.2 eV, 496.5 eV and 530.5 eV are attributed to Cl 2p, C 1s, Sn 3d and O1s of antTiO<sub>2</sub>-CH, respectively. In spectrum (b), the characteristic peak seen at 398.5 eV is assigned to the presence of N 1s present in the bienzyme (ChEt-ChOx). The additional peak found at 1069.5eV is attributed to Ti-Auger. The relative atomic concentration (%) and full width half maxima (FWHM) of carbon, oxygen and nitrogen peaks are summarized in Table S1 (Supporting Information). The atomic concentration of N 1s of ChEt-ChOx/antTiO<sub>2</sub>-CH/ITO bioelectrode increases to 2.48% as compared to that of antTiO<sub>2</sub>-CH/ITO electrode (1.23%). This indicates that antTiO<sub>2</sub>-CH/ITO electrode surface facilitates immobilization of ChEt-ChOx via electrostatic interactions.

The XPS spectra of the carbon 1s region, obtained for the deposited antTiO<sub>2</sub>-CH/ITO electrode [Figure 3(ii)], is deconvoluted using Shirley type baseline and Lorentzian-Doniac-

Sunsi curves with Gaussian profile. The deconvoluted C1s core-level spectrum of antTiO<sub>2</sub>-CH sample consists of three peaks. The 284.5 eV peak is assigned to the existence of the C-C and C-N binding in CH. The second peak, located at 286.3eV, is attributed to the chemical binding of the C atom in C-O and C-OH bonds, and the third peak seen at 288.06 eV, is related to the N-C=O chemical binding in the acetamide group of CH. After bienzyme immobilization, the peaks found at 284.5 eV, 286.3eV and 288.06 eV are slightly shifted towards the lower binding energy and an additional peak at 281.8 eV is observed [Figure 1(iii)]. After fitting of the N1s core-level spectrum of antTiO<sub>2</sub>-CH, three peaks appear at 398.3, 401.4, and 406.2 eV [Figure 1(iv)]. The first peak is assigned to the chemical binding of N in the amine and acetamide (NH<sub>2</sub>) groups, while the second peak is assigned to the chemical binding of the N in the protonated amine (NH<sub>3</sub><sup>+</sup>) group. The third peak is attributed to chemical binding of the N in the nitrate group. In case of the biofunctionalized film, these peaks are slightly shifted towards the higher binding energy [Figure 1(v)]. The atomic ratio of element (N) and peak intensity is found to be changed indicating bienzyme immobilization onto antTiO<sub>2</sub>-CH surface via electrostatic interactions.

Figure S1 (i and ii) shows the Ti2p core level spectra of antTiO<sub>2</sub>-CH film before and after enzyme immobilization. The peaks seen at around 454.4, 457.6 and 459.4 eV are responsible for various oxidation states of titatium such as Ti<sup>2+</sup>, Ti<sup>3+</sup> (intermediate oxidation state) and Ti<sup>4+</sup> (higher oxidation state) , respectively. A peak seen at 464.7 eV arising due to Ti2p<sub>1/2</sub> in the antTiO<sub>2</sub>-CH film has been shifted to 2.0 eV after enzyme incorporation. A new peak has been observed at 452.3 eV due to low oxidation state of titanium (Ti<sup>0</sup>) [Figure S1(ii)]. Some of the peaks for Ti<sup>2+</sup> and Ti<sup>3+</sup> have been shifted due to surface functionalization antTiO<sub>2</sub>-CH/ITO with enzyme molecules [Figure S1(ii)]. In addition Ti<sup>4+</sup> with TiO<sub>2</sub>, other lower oxidation states are related to TiO<sub>2</sub> due to the presence of titanium suboxides. Thus, existence of these peaks Ti<sup>0</sup>, Ti<sup>2+</sup>, Ti<sup>3+</sup> etc. may result in defects in the atomic structure of mesoporous anatase TiO<sub>2</sub> resulting in improved heterogeneous electron transfer properties and enhanced loading capacity of the enzyme molecules.

FT-IR spectra of antTiO<sub>2</sub>/ITO exhibits a peak at 523 cm<sup>-1</sup> in the finger print region due to vibrational band of Ti-O bond [Figure 3(vi), spectra a]. The peaks found at 819 and 1241 cm<sup>-1</sup> correspond to C-H and C-O stretching bonds, respectively. The band seen at 3593 cm<sup>-1</sup> is assigned to stretching and deformation of the O-H bond due to absorption of the water molecules. Figure 3(vi) shows FT-IR spectra of CH (spectra b) that exhibits bands at 3200-3450

$\text{cm}^{-1}$  due to the stretching vibration mode of OH and  $\text{NH}_2$  groups. The band seen at  $1652 \text{ cm}^{-1}$  arises due to amide I group (C–O stretching along with N–H deformation mode). The  $1564 \text{ cm}^{-1}$  peak is attributed to  $\text{NH}_2$  group due to N–H deformation,  $1400 \text{ cm}^{-1}$  peak is due to C–N axial deformation (amine group band),  $1317 \text{ cm}^{-1}$  peak is due to  $\text{COO}^-$  group in the carboxylic acid salt and  $1063 \text{ cm}^{-1}$  is attributed to the stretching vibration mode of the hydroxyl group. The peak at  $612 \text{ cm}^{-1}$  in the finger print region is assigned to antTiO<sub>2</sub> grafted CH. This absorption band occurs at the higher wavenumber than that of the pure antTiO<sub>2</sub> nanoparticles due to the interactions between CH and the antTiO<sub>2</sub>. The presence of antTiO<sub>2</sub> nanoparticles in CH facilitates immobilization of ChEt–ChOx via amine and hydroxyl group. After immobilization of ChEt–ChOx on antTiO<sub>2</sub>–CH surface (spectra c), intensity of the absorption peak becomes higher and broader due to overlap of the functional groups of enzymes corresponding to amide I ( $1652 \text{ cm}^{-1}$ ) and amide II ( $1545 \text{ cm}^{-1}$ ), respectively, indicating immobilization of the bienzyme (ChEt–ChOx) onto this matrix.

The specific surface area and porosity of the TiO<sub>2</sub> and antTiO<sub>2</sub>–CH have been studied by using the N<sub>2</sub> adsorption and desorption isotherms shown in Figure 4a. Table 1 shows the pore size distribution of the TiO<sub>2</sub> and antTiO<sub>2</sub>–CH from Brunauer–Emmett–Teller (BET) measurements. It is found that the two isotherms of samples show the stepwise adsorption and desorption pertaining to type IV curves, representing the presence of nanoporous material. A hysteresis loop with a stepwise adsorption and desorption branch is observed in the extensive range of pressure ( $P/P_0$ ) for the nanoporous TiO<sub>2</sub> and antTiO<sub>2</sub>–CH indicating that the synthesized material has nanoporous structure. To investigate the pore size and pore volume distribution, a curve of the pore size distribution is inspected by desorption branch of the Barrett–Joyner–Halenda (BJH) data as shown in the inset of the Figure 4a. The average pore diameter of mesoporous TiO<sub>2</sub> is found to be as 6.287 nm with ~80% mesoporosity and total pore volume of 0.2961cc/g. The total pore volume of mesoporous antTiO<sub>2</sub>–CH is 0.1265 cc/g and the mesoporosity is 83%. Analyzing BET results, it is seen that titania nanoparticles have an increased surface area of  $188.2 \text{ m}^2/\text{g}$  compared to that of antTiO<sub>2</sub>–CH ( $90.83 \text{ m}^2/\text{g}$ ). The decrease in surface area of antTiO<sub>2</sub>–CH is evident because of the blocking of pore entrances of TiO<sub>2</sub> particles by the chitosan molecules.

Figure 4b illustrates the room temperature Raman spectra of the  $\text{TiO}_2$  and  $\text{antTiO}_2\text{-CH}$ . The resultant spectra indicate intensification of the lowest-frequency  $E_g$  mode. A strong Raman peak emerges at  $196\text{ cm}^{-1}$  at the high-frequency side of the  $E_g$  mode assigned to the anatase phase of  $\text{TiO}_2$ . In addition,  $B_{1g}$ ,  $A_{1g}$  and  $E_g$  modes are detected at  $396$ ,  $517$  and  $642\text{ cm}^{-1}$ , respectively indicating the presence of anatase phase. It appears that the morphology of  $\text{TiO}_2$  in the  $\text{antTiO}_2\text{-CH}$  phase is preserved.

### Electrochemistry and Microfluidics

Figure 5(i) shows the cyclic voltammogram of (a)  $\text{antTiO}_2\text{-CH/ITO}$  electrode and (b)  $\text{ChEt-ChOx/antTiO}_2\text{-CH/ITO}$  bioelectrode in the potential range of  $-0.9\text{ V}$  to  $+1.0\text{ V}$  conducted in PBS containing  $5\text{ mM} [\text{Fe}(\text{CN})_6]^{3-/4-}$ . The magnitude of current observed for the  $\text{ChEt-ChOx/antTiO}_2\text{-CH/ITO}$  bioelectrode is higher (curve b) as compared to that of the  $\text{antTiO}_2\text{-CH/ITO}$  electrode (curve a) resulting in fast electron communication through  $\text{antTiO}_2\text{-CH}$  and redox active site of  $\text{ChEt-ChOx}$  molecules. Ali *et al.* reported that  $\text{antTiO}_2$  nanoparticles can be used to activate the enzyme resulting in reduced tunneling distance for diffusion of electrons from the bulk solution leading to enhanced current.<sup>26</sup> Li *et al.* have observed that the current response increases after enzyme immobilization on  $\text{TiO}_2$  nanodots in the presence of gibbosities on  $\text{TiO}_2$  surface resulting in decreased tunneling distance between active site of  $\text{ChOx}$  and the electrode.<sup>35</sup> This result indicates that porous CH with  $\text{antTiO}_2\text{-CH}$  facilitates activation of enzyme active sites resulting in enhanced current due to improved heterogeneous electron transfer. The high electrocatalytic activity of  $\text{antTiO}_2$  in presence of the bienzyme reveals improved redox phenomenon. The observed significant increase in the heterogeneous electron transfer rate results due to strong interaction of  $\text{ChEt-ChOx}$  with nanoporous  $\text{antTiO}_2\text{-CH}$  based electrode as compared to that of  $\text{antTiO}_2\text{-CH/ITO}$  electrode. The effect of the scan rate on the electrochemical response of bioelectrode is shown in Figure S2 (Supplementary). The magnitude of current increases linearly with the increase of scan rate from  $20$  to  $160\text{ mVs}^{-1}$  (inset). Besides this, the  $\text{ChEt-ChOx/antTiO}_2\text{-CH}$  bioelectrode shows that the peak current increases linearly with scan rate ( $20\text{-}110\text{ mV/s}$ ) indicating surface confined electron-transfer process [Supplementary, Figure S2(inset)]. The observed large separation voltage ( $\sim 1.0\text{ V}$ ) of CV may be attributed to the irreversible electrode process or large ohmic drop in the electrochemical cell. The diffusion coefficient (or diffusivity) of the electrolyte containing  $[\text{Fe}(\text{CN})_6]^{3-/4-}$  ions from CV response at different scan rate has been estimated. The observed fast response time may be assigned to the

higher diffusivity ( $76.37 \times 10^{-6} \text{ cm}^2/\text{s}$ ) of the redox species at the ChEt-ChOx/antTiO<sub>2</sub>-CH/ITO bioelectrode.

The effect of flow rate of the nonporous antTiO<sub>2</sub>-CH based microfluidic biochip has been investigated using chronoamperometric technique. Figure 5(ii) shows chronoamperometric response of the antTiO<sub>2</sub>-CH/ITO electrode (a) and ChEt-ChOx/antTiO<sub>2</sub>-CH/ITO (b) as a function of flow rate (0.01-15  $\mu\text{L}/\text{min}$ ). It has been observed, that the chronoamperometric current increases with increasing flow rate (buffer solution) upto 5  $\mu\text{L}/\text{min}$  after which the current becomes saturated (curve a). This is because diffusivity of the redox species increases with higher buffer flow rate due to improved mass transport resulting from the increased fluid velocity. The corresponding chronoamperometric curves are shown in Figure S3 (Supplementary). In case of the ChEt-ChOx/antTiO<sub>2</sub>-CH/ITO bioelectrode [Figure 3(ii)(b) and Supplementary, Figure S4], it is found that the current initially rises with flow rate (buffer solution plus cholesterol; 25 mg/dl) upto 1.0  $\mu\text{L}/\text{min}$  after which it decreases to a saturated value. This may be assigned to the biochemical reaction at the sensor surface. It appears that the cholesterol molecules perhaps move away from the sensor surface prior to completion of the biochemical reaction resulting in decreased current. Thus, the electrochemical measurements have been carried out at the optimum flow rate of 1.0  $\mu\text{L}/\text{min}$ .

### Electrochemical Impedance Analysis

Electrochemical impedance is a complex resistance and is encountered when the current flows through the circuit consisting of resistors and capacitors or inductors.<sup>1-4</sup> The Randles circuit [Schematic 1(iii)] is an equivalent electrical circuit that is commonly used to measure electrochemical impedance comprising of an active electrolyte resistance  $R_s$  in series with  $R_{ct}$  (charge transfer resistance) in parallel combination of the double-layer capacitance  $C_{dl}$  or constant phase element (CPE) of a Faradaic reaction.<sup>5</sup> A typical shape of Nyquist plot includes a semicircle region lying on the real axis followed by a straight line. The linear part ( $\psi = \pi/4$ ), observed in the low frequency range implies a mass-transfer limited process, whereas the semicircle portion observed in the high frequency range, implies a charge-transfer limited process. Both Nyquist and Bode plots have been used to determine the relative change in surface-charge resistance. Interfacial  $R_{ct}$  and  $C_{dl}$  in Nyquist plot of impedance are obtained from

real ( $Z'$ ) and imaginary ( $-Z''$ ) impedance as a function of frequency using the following Eq. 1 for a parallel RC circuit.

$$Z(\omega) = R_s + \frac{R_{ct}}{1+j\omega R_{ct}C_{dl}} = R_s + \frac{R_{ct}}{1+\omega^2 R_{ct}^2 C_{dl}^2} - \frac{j\omega R_{ct}^2 C_{dl}}{1+\omega^2 R_{ct}^2 C_{dl}^2} = Z' + jZ'' \quad \text{Eq.1}$$

where,  $R_s$  is the electrolyte solution resistance and  $R_{ct}$  is the charge transfer resistance or polarization resistance. The frequency associated with maximum  $-Z''$  and  $R_{ct}$  are used to calculate  $C_{dl}$  using the following Eq. 2.

$$R_{ct}C_{dl} = \frac{1}{2\pi f_{max}} = \tau \quad \text{Eq. 2}$$

where,  $\tau$  is the time constant and  $f_{max}$  is the maximum frequency. The Warburg resistance ( $Z_w$ ) can be obtained via the Nyquist plot and an equivalent circuit to describe the electrical response at electrode. In the plot, the Warburg impedance is expressed by an intercept of straight line having a slope of unity and can be derived via Eq. 3.

$$Z_w(\omega) = W_{int} + \left(\frac{R_{ct}\lambda}{\sqrt{2}\omega}\right) [1 - j]; \quad W_{int} = R_s + R_{ct} - R_{ct}^2\lambda^2 C_d \quad \text{Eq.3}$$

where,  $\lambda = \left(\frac{k_f}{\sqrt{D_0}} + \frac{k_b}{\sqrt{D_R}}\right)$ ,  $k_f$  and  $k_b$  are forward and backward electron-transfer rate constants,  $D_0$  and  $D_R$  are the diffusion coefficient of oxidant and reductant. The  $R_s$  and  $R_s + R_{ct}$  values are obtained from standard software available with the instrument. Similar information is obtained from Bode diagram of impedance and phase shift with frequency.

The charge transfer resistances,  $R_{ct1}$  and  $R_{ct2}$  for both the circuits of antTiO<sub>2</sub>-CH/ITO electrode have been found to be as 22.0 k $\Omega$  and 3.1  $\times 10^5 \Omega$ , respectively at 0.6V bias potential [Figure 5(iii), (a)]. It appears that the nanoporous antTiO<sub>2</sub>-CH matrix in this biochip plays an important role for fast electron transfer from the bulk solution to electrode. In particular, experimentally obtained  $R_{ct}$  in the antTiO<sub>2</sub>-CH matrix may be due to diffusion of the antTiO<sub>2</sub> nanoparticles in CH network resulting in increased conductivity and compensation for the observed higher resistance of CH due to larger molecules. The  $R_{ct}$  further decreases ( $R_{ct1}$ =16.8 k $\Omega$  and  $R_{ct2}$ =2.7  $\times 10^5 \Omega$  for both equivalent circuits) after the immobilization of ChEt-ChOx onto antTiO<sub>2</sub>-CH surface revealing that antTiO<sub>2</sub>-CH provides a desirable microenvironment for the immobilization of the bienzyme [Figure 3(iii), (b)]. Thus, the ChEt-ChOx/antTiO<sub>2</sub>-CH/ITO

bioelectrode provides easier electron transfer due to increased active sites for electrical contact between electrode and the redox label in solution resulting in lower electrochemical impedance.

Figure S5 shows EIS spectra of nanopore microfluidic biochip obtained as a function of flow rate (0.01- 5  $\mu\text{L}/\text{min}$ ) (Supplementary). It is observed that  $R_{ct2}$  of the semicircle gradually increases, with increased flow rate of cholesterol solution containing  $[\text{Fe}(\text{CN})_6]^{3-/4-}$  ions. This may be due to increased number of  $[\text{Fe}(\text{CN})_6]^{3-/4-}$  ions at the higher fluid velocity. After 1.0  $\mu\text{L}/\text{min}$ , the impedance of ChEt-ChOx/antTiO<sub>2</sub>-CH/ITO bioelectrode increases slowly and becomes saturated [Supplementary, Figure S5(inset)]. This optimum flow rate of 1.0  $\mu\text{L}/\text{min}$  has been used to conduct EIS measurements.

Figure 6(i) shows EIS spectra of the fabricated biochip as a function of potential (0 – 0.7 V). It can be seen that the two semicircles appear in the low frequency region and high frequency region as shown in the equivalent circuit model. The  $R_{ct2}$  values of semicircle 2 in low frequency region of the ChEt-ChOx/antTiO<sub>2</sub>-CH/ITO bioelectrode have been found to increase linearly with increased potential [inset, Figure 6(ii)]. This reveals facile electron transfer kinetics wherein resistance controls the electron transfer kinetics of the redox probe at the electrode. The depression angle ( $\delta$ ) is an important parameter by which the semicircular displaced below the real axes is related to the width of the relaxation time distribution<sup>6</sup>. It can be seen that arc of the semicircle with least  $\delta$  value, is less distorted from centre of the real axis and can be estimated using the relation  $\delta = (1 - n)\pi/2$  where,  $n$  is the fractional exponent. Figure S6(i) shows the variation of depression angle ( $\delta$ ) for ChEt-ChOx/antTiO<sub>2</sub>-CH/ITO bioelectrode as a function of applied potential (Supplementary). It has been found that the  $\delta$  value for the microfluidic biochip decreases with increasing the potential from 0 to 0.7 V. The electric double layer or constant phase element ( $C_{dl}$ ) has been found to decrease with increasing potential [Supplementary, Figure S6(ii)]. It suggests that the resistance as represented in the semicircle of the Nyquist plot depends on the bias voltage. Thus, the  $R_{ct2}$  value increases at higher potential indicating that the charge transfer at low frequency is dependent on polarization potential. Thus, 0.6V has been chosen for biosensing. This higher potential may be attributed to the large gap between working and reference electrodes resulting in higher ohmic of potential.

The nanopore microfluidic biochip is characterized by analyzing the following important parameters such as heterogeneous electron transfer rate constant ( $k_0$ ) and time constant ( $\tau$ ) for

redox probe containing  $[\text{Fe}(\text{CN})_6]^{3-/4-}$  ions.<sup>6</sup> These studies allow interfacial interaction of biomolecules as well as help in the characterization of the structural features of the sensing interface and for explaining the mechanism of chemical processes occurring at the electrode/solution interfaces. The corresponding  $k_0$  of the modified electrode has been calculated using charge transfer kinetics,  $k_0 = RT/n^2F^2AR_{ct2}C$ , where  $R$  is the gas constant,  $T$  is the temperature,  $n$  is the electron transferring constant of the redox couple,  $F$  is Faraday constant,  $A$  is the effective area of the electrode, and  $C$  is the concentration of the redox couple in the bulk solution. The  $k_0$  value of the ChEt-ChOx/antTiO<sub>2</sub>-CH/ITO bioelectrode obtained as  $2.03 \times 10^{-6}$  cm/s is higher than that for antTiO<sub>2</sub>-CH/ITO electrode ( $1.7 \times 10^{-6}$  cm/s), indicating faster electron exchange between the redox species. The ChEt-ChOx immobilization on antTiO<sub>2</sub>-CH shows a sluggish electron charge transfer rate constant resulting in generation of the low capacitance at the electrode surface. The high value of time constant ( $\tau$ ) for the ChEt-ChOx/antTiO<sub>2</sub>-CH compared to that of the mesoporous antTiO<sub>2</sub>-CH electrode is observed due to the slow diffusion of  $[\text{Fe}(\text{CN})_6]^{3-/4-}$  ions at the electrode enzyme layer/solution interface. The surface coverage ( $\theta$ ), is calculated using the relation

$$\theta = 1 - \frac{R_{ct2(\text{electrode})}}{R_{ct2(\text{bioelectrode})}} \quad \text{Eq. 4}$$

where,  $\theta$  is the fraction of occupied binding sites. The  $R_{ct2(\text{electrode})}$  and  $R_{ct2(\text{bioelectrode})}$  are the surface specific charge transfer resistances of antTiO<sub>2</sub>-CH electrode and ChEt-ChOx/antTiO<sub>2</sub>-CH bioelectrode, respectively. The value of  $\theta$  has been determined to be as 0.87, indicating more than 87% of the surface coverage of the antTiO<sub>2</sub>-CH electrode by ChEt-ChOx molecules.

### Biomedical Application

The electrochemical impedimetric response of the nanopore microfluidic biochip obtained as a function of cholesterol concentration (2–500 mg/dl) in PBS solution containing  $[\text{Fe}(\text{CN})_6]^{3-/4-}$  is shown in Figure 6(ii). During the electrochemical measurements, various concentrations of cholesterol are injected into the microchannels at a optimum flow rate of 1.0  $\mu\text{l}/\text{min}$ . A Faradic impedance spectrum (Nyquist plot) includes two semicircle regions observed at higher and lower frequencies corresponding to electron-transfer limited process. The electronic impedimetric circuit of the electrochemical system has been shown in Schematic 1(iii). It can be seen that change in the second semicircle diameter ( $R_{ct2}$ ) is higher compared to that of the first semicircle

as shown in Figure 6(ii). The charge transfer resistance of microfluidic ChEt-ChOx/CH-antTiO<sub>2</sub>/ITO bioelectrode ( $R_{ct2}$ ) reveals electron-transfer kinetics of redox probe at the electrode interface which decreases with increasing cholesterol oleate concentration [Supplementary, Figure S7]. This can be attributed to the presence of ChEt on antTiO<sub>2</sub>-CH/ITO electrode. The esterified cholesterol converts cholesterol into cholesterol and fatty acid. Again, ChOx converts cholesterol to choleste-4-ene-3-one and H<sub>2</sub>O<sub>2</sub>. The generated electrons during the re-oxidation of ChOx after enzymatic reaction are transferred to the antTiO<sub>2</sub>-CH/ITO electrode via redox couples resulting in enhanced charge transfer rate leading to decreased  $R_{ct2}$  value. A linear calibration curve [Figure 6(iii)] has been fitted between  $R_{ct2}$  and logarithm of cholesterol concentration revealing linearity from 2 to 400 mg/dl in the detection range of 2-500 mg/dl. The linear regression equation is  $R_{ct2}(\Omega) = 27.9 \text{ k}\Omega - 6.77 \text{ k}\Omega \text{ mg}^{-1}\text{dl} \times [\text{Cholesterol oleate concentration (mg/dl)}]$  with a correlation coefficient of 0.996. The nanopore antTiO<sub>2</sub>-CH based microfluidic chip yields excellent sensitivity (67.7 k $\Omega$ /mg/dl) compared to those reported in literature.<sup>6</sup> The sensitivity of the present nanoporous antTiO<sub>2</sub>-CH microelectrode based impedance enzymatic sensor is several-folds higher, revealing that coupling of the microfluidic impedance sensor with biopolymer-nanostructured microelectrode provides a technology for more sensitive detection of esterified cholesterol. In addition, the density of point defects in the nanopore anatase TiO<sub>2</sub> may influence electrochemical conduction between enzyme molecules and electrode, and facilitates heterogeneous electron transfer resulting in higher sensitivity. The low apparent Michaelis–Menten constant ( $K_m^{app}$ ) obtained as 1.3 mg/dl as compared to other bioelectrodes<sup>36-39</sup> indicates that the nanoporous antTiO<sub>2</sub>-CH based bioelectrode has higher affinity towards the esterified cholesterol. The chitosan can act as a bio-linker between enzyme and nanopore TiO<sub>2</sub> nanoparticles which has improved the loading capacity of enzyme molecules due to the available functional groups (-NH<sub>2</sub>, -OH etc.). As compared to other cholesterol biosensors (Table 2),<sup>6,26,36-39</sup> this proposed impedimetric microfluidic biochip shows a lower detection limit of 0.2 mg/dl and a wide detection range of 2-500 mg/dl. The biosensing characteristics of nanopore microfluidic biochip along with those reported in literature are summarized in Table 2.

The reproducibility of the nanopore microfluidic device has been investigated with 100 mg/dl cholesterol plus buffer solution. The ChEt-ChOx/antTiO<sub>2</sub>-CH/ITO bioelectrode shows good repeatability as evidenced by RSD of 2.2 % (n = 15) for 100 mg/dl cholesterol

concentration, after 15 times washing/repetition of the bioelectrode. No significant decrease in  $R_{ct2}$  value is observed after 12 times after which the bioelectrode shows slight decrease in current response arising may be due to denaturation of biomolecules.

The shelf-life of the nanopore microfluidic biochip measured after an interval of 1 week has been estimated to be 8 weeks. The decrease in the value of  $R_{ct2}$  has been found to be about 10% up to about 8 weeks after which the  $R_{ct2}$  decreases resulting in about 80% loss in about 10 weeks. The specificity of this enzymatic sensor is mainly dependent upon the bienzyme (ChEt-ChOx) immobilized on the sensor surface. To evaluate the specificity of the nanopore antTiO<sub>2</sub>-CH based impedance enzymatic sensor, glucose (5 mM), uric acid (0.1 mM), and urea (1 mM) analytes present in human serum sample, are tested at a concentration of 100 mg/dl (cholesterol oleate) using CV. No significant change in current response has been found as indicated by low RSD of 4.4 % (Supplementary, Figure S8). The higher enzyme adsorption on nanoporous antTiO<sub>2</sub>-CH composite is thus improved the detection limit, range and selectivity of this microfluidic biosensor. Thus, the EIS method of detection and the integration of nanopore antTiO<sub>2</sub>-CH matrix to the microfluidic device is an efficient, fast and low cost technique for total cholesterol detection.

## Conclusion

We have fabricated a nanopore microfluidic biochip based on dispersive nanostructured antTiO<sub>2</sub> nanoparticles grafted CH for detection of cholesterol molecules. The morphological (AFM, SEM) and spectroscopic (Raman, FT-IR, XPS) investigations of nanoporous antTiO<sub>2</sub>-CH matrix indicate surface functionalization of ChEt-ChOx. Around 57.2 % of total pore volume decreases (i. e. from 0.2961 cc/g to 0.1265 cc/g of pore volume) after chitosan incorporation in nanopore anatase titania and the surface area decreases due to blocking of the pore entrances. Using an impedance approach, we have investigated the impedance change due to catalytic reaction of enzymes cholesterol detection using antTiO<sub>2</sub>-CH based microfluidic biochip. The impedance analysis of this microfluidic device offers small instrument size, low reagent consumption, and system automation, indicating that this microfluidic device has a high potential for clinical applications. Presence of defects (Ti<sup>3+</sup>, Ti<sup>2+</sup>, Ti<sup>0</sup> etc.) in nanopore antTiO<sub>2</sub> may be responsible for higher sensitivity, low detection limit and improved stability of the fabricated microfluidic chip. The improved biosensor characteristics can be explained by the high electronic conductivity of

nanoporous antTiO<sub>2</sub>-CH and good catalytic activity of the nanoparticles. The presence of CH not only enhances the electrode forming ability but also improves dispersion of antTiO<sub>2</sub> nanoparticles at the surface. In the future, this microfluidic biochip with the nanopore antTiO<sub>2</sub>-CH electrode may prove to be an efficient platform for the diagnostics of other clinically important analytes such as glucose, urea, lipids, *etc.*

## Materials and Methods

### Biochip Design

The PDMS microchannels of desired dimensions (2cm×200μm×200μm) were fabricated using soft lithographic.<sup>26</sup> The inlet and outlet were fabricated by punching holes at the ends of the microchannel. Two patterned microelectrodes comprising of dimensions (0.2×2.5 cm<sup>2</sup>) have been prepared on ITO coated glass slide of size 2.5×3.5 cm<sup>2</sup> by photolithography. The ITO glass is cleaned with acetone prior to use. First, we spin-coated the positive photoresist (Shipley 1811) onto ITO glass substrate with 3000 rpm for 20s. In order to remove the solvent, the photoresist coated substrate was soft baked using a hot plate for 1 min. Then, the substrate was exposed to UV radiation for about 5 min through a given optical mask (high resolution black printed transparent sheet). The substrate was dipped into a positive photoresist developer solution for 10s to develop the pattern. Lastly, the chemical ITO etchant (Zinc dust + HCL solution 15%) was used to etch ITO from exposed region. The remaining photoresist on ITO after ITO etching was removed by acetone. This patterned ITO electrode was then cleaned with acetone via sonication (10 min), later with dichloromethane (10 min), and finally with water for several times. These clean electrodes were placed in a vial wherein a mixture of H<sub>2</sub>O:H<sub>2</sub>O<sub>2</sub> (30%):NH<sub>3</sub> (25%) (5:1:1) is added and stirred for 1 h at 70<sup>0</sup>C. Then, the slides were washed with plenty of water and dried in an oven at 100<sup>0</sup>C for 4 h.

A CH (0.50%) solution was prepared by dissolving CH (50 mg) in 100 mL of acetate buffer (0.05 M, pH 4.2) solution. The precursor material titanium (IV) butoxide was dissolved in 2-methoxy ethanol in order to prepare 5(wt %) sol gel using de-ionized H<sub>2</sub>O and nitric acid treatment under continuous stirring. After hydrolysis, the thick sol was kept for aging at an intermediate temperature ~110<sup>0</sup>C for half an hour. Finally, the sol was annealed at 450<sup>0</sup>C for 2 h in air atmosphere to obtain antTiO<sub>2</sub> nanoparticles. The calculated amount of antTiO<sub>2</sub> nanoparticles was dispersed in the CH solution (5 mg/ml) by stirring at room temperature after

which it was ultra-sonicated. A highly viscous solution of CH with uniformly dispersed antTiO<sub>2</sub> nanoparticles was thus obtained. The selective deposition of antTiO<sub>2</sub>-CH solution has been carried out on this fabricated patterned ITO electrode via dip coating. Initially, the glass substrate with ITO microelectrode was masked using a tape and only the desired electrode was selectively exposed by removing the masking tape over it. The substrate was then dried at 40°C for about 1 h after which the remaining masking tape film was removed from the substrate. This process resulted in a glass substrate containing antTiO<sub>2</sub>-CH/ITO (unmasked region) and bare ITO electrode (masked region). The antTiO<sub>2</sub>-CH/ITO film was washed with deionized water to remove any loosely bound particles.

### Surface Functionalization

The fresh solution was prepared by mixing 1mg/ml cholesterol esterase (ChEt) and 1mg/ml cholesterol oxidase (ChOx) in PBS buffer in the ratio 1:1. 10µl solution of this mixture was uniformly spread onto antTiO<sub>2</sub>-CH surface via physical absorption [Schematic 2] and kept in a humid chamber for about 12 h at 4°C. The surface charged antTiO<sub>2</sub> nanoparticles interacted with -NH<sub>2</sub>/OH groups of CH [cationic amine-rich polysaccharide (pH 4.2)] via electrostatic interactions and hydrogen bonding. The bienzyme ChEt-ChOx being negatively charged at pH 7.0 could be immobilized on the positively charged antTiO<sub>2</sub>-CH via electrostatic interactions. This ChEt-ChOx/antTiO<sub>2</sub>-CH based bioelectrode was washed with 50 mM PBS (pH 7.0) in order to remove any unbound enzymes from the electrode surface. The bioelectrode was stored at 4 °C when not in use. It has been found that the ChEt-ChOx/antTiO<sub>2</sub>-CH/ITO bioelectrode shows high catalytic behavior in phosphate buffer at pH 7.4 (50mM, 0.9% NaCl) containing [Fe(CN)<sub>6</sub>]<sup>3-/4-</sup> (5mM). The PDMS microchannel was reversibly sealed to a glass substrate comprising of ITO electrode and ChEt-ChOx/antTiO<sub>2</sub>-CH/ITO bioelectrode, respectively. The inlet reservoir of microchannel was used to introduce the syringe pump to maintain flow rate at 1 µL/min. An Ag/AgCl wire introduced to the outlet reservoir of microchannel acts as a reference electrode and the bare ITO microelectrode serves as the counter electrode [Schematic 1(i and ii)].<sup>26</sup> The various steps relating to the fabrication of the microfluidic device are shown in Schematic 2. During cholesterol detection, the unreacted reactants were removed by washing microchannels with help of phosphate buffer for each concentration of cholesterol.

## References

- 1 K. -H. Lee, J. -O. Lee, M.-J. Lee, B. Sohn, S.-H. Choi, S. K. Kim, J.-B. Yoon, G.-H. Cho, *Biosen. Bioelectron.* 2010, **26**, 1373–1379.
- 2 F. Lisdat, D. Schäfer, *Anal. Bioanal. Chem.* 2008, **391**, 1555–1567.
- 3 J.-J. Wu, D. K.-P. Wong, *Adv. Mater.* 2007, **19**, 2015–2019.
- 4 J. S. Daniels, N. Pourmand, *Electroanalysis* 2007, **19**, 1239–1257.
- 5 A. Bonanni, M. del Vallea, *Anal. Chim. Acta* 2010, **678**, 7–17.
- 6 A. Kaushik, P. R. Solanki, K. Kaneto, C. G. Kim, S. Ahmad, B. D. Malhotra, *Electroanalysis* 2010, **22**, 1045 – 1055.
- 7 P. Neuzil, S. Giselbrecht, K. Länge, T. J. Huang, A. Manz, *Nat. Rev. Drug. Discov.* 2012, **11**, 621.
- 8 V. N. Goral, P. K. Yuen, *Ann. Biomed. Eng.* 2012, **40**, 1244–1254.
- 9 T. Vilkner, D. Janasek, A. Manz, *Anal. Chem.* 2004, **76**, 3373–3385.
- 10 D. J. Harrison, K. Fluri, K. Seiler, Z. Fan, C. S. Effenhauser, A. Manz, *Science* 1993, **261**, 895-897.
- 11 A. C. R. Grayson, R. S. Shawago, M. J. Johnson, N. T. Flynn, Y. Li, M. J. Chima, R. Langer, *Proc. IEEE* 2004, **92**, 6-21.
- 12 H. Becker, C. Gartner, *Electrophoresis* 2000, **21**, 12-26.
- 13 L. Gervais, E. Delamarche, *Lab Chip* 2009, **9**, 3330–3337.
- 14 S. K. Sia, G. M. Whitesides, *Electrophoresis* 2003, **24**, 3563–3576.
- 15 Z. Nie, C. A. Nijhuis, J. Gong, X. Chen, A. Kumachev, A. W. Martinez, M. Narovlyansky, G. M. Whitesides, *Lab on a Chip* 2010, **10**, 477-483.
- 16 S. K. Arya, G. Chornokur, M. Venugopal, S. Bhansali, *Analyst* 2010, **135**, 1941–1946.

- 17 Y. B. Hahn, R. Ahmad, N. Tripathy, *Chem. Commun.* 2012, **48**, 10369-10385.
- 18 P. R. Solanki, A. Kaushik, V. V. Agrawal, B. D. Malhotra, *NPG Asia Mater.* 2011, **3**, 17-24.
- 19 G. Shen, P.C. Chen, K. Ryu, C. Zhou, *J. Mater. Chem.* 2009, **19**, 828–839.
- 20 E. S. Kwak, W. Lee, N.-G. Park, J. Kim, H. Lee, *Adv. Funct. Mater.* 2009, **19**, 1093–1099.
- 21 S. Yurdakal, G. Palmisano, V. Loddo, V. Augugliaro, L. Palmisano, *J. Am. Chem. Soc.* 2008, **130**, 1568-1569.
- 22 D. Chen, F. Huang, Y.-B. Cheng, R. A. Caruso, *Adv. Mater.* 2009, **21**, 2206–2210.
- 23 J. Wang, Y. Zhou, Y. Hu, R. O’Hayre, Z. Shao, *J. Phys. Chem. C* 2011, **115**, 2529–2536.
- 24 J. Cui, D. Sun, S. Chen, W. Zhou, P. Hu, H. Liu, Z. Huang, *J. Mater. Chem.* 2011, **21**, 10633.
- 25 R. Wang, C. Ruan, D. Kanayeva, K. Lassiter, Y. Li, *Nano Lett.* 2008, **8**, 2625-2631.
- 26 Md. A. Ali, S. Srivastava, P. R. Solanki, V. V. Agrawal, R. John, B. D. Malhotra, *Appl. Phys. Lett.* 2012, **101**, 084105.
- 27 H. G. Yang, C. H. Sun, S. Z. Qiao, J. Zou, G. Liu, S. C. Smith, H. M. Cheng, G. Q. Lu, *Nature*, 2008, **453**, 638-641.
- 28 H. B. Jiang, Q. Cuan, C. Z. Wen, J. Xing, D. Wu, X.-Q. Gong, C. Li, H. G. Yang, *Angew. Chem. Int. Ed.* 2011, **50**, 3764 –3768.
- 29 P. Xiaoa, Y. Zhangb, G. Cao, *Sensors Actuators B* 2011, **155**, 159–164.
- 30 A. C. Papageorgiou, N. S. Beglitis, C. L. Pang, G. Teobaldi, G. Cabailh, Q. Chen, A. J. Fisher, W. A. Hofer, G. Thornton, *Proc. Natl. Acad. Sci.* 2010, **107**, 2391–2396.
- 31 K.-J. Feng, Y.-H. Yang, Z.-J. Wang, J.-H. Jiang, G.-L. Shen, R.-Q. Yu, *Talanta* 2006, **70**, 561–565.
- 32 E.J. W. Crossland, N. Noel, V. Sivaram, T. Leijtens, H. J. A.-Webber, H. J. Snaith, *Nature* 2013, **495**, 215-219.

- 33 T. Wagner, S. Haffer, C. Weinberger, D. Klaus, M. Tiemann, *Chem. Soc. Rev.* 2013, **42**, 4036-4053.
- 34 H. Li, T.-Y. Ma, D.-M. Kong, Z.-Y. Yuan, *Analyst* 2013, **138**, 1084-1090.
- 35 Q. Li, K. Cheng, W. Weng, P. Du, G. Han, *J. Mater. Chem.* 2012, **22**, 9019-9026.
- 36 B. D. Malhotra, A. Kaushik, *Thin Solid Films* 2009, **518**, 614-620.
- 37 A. A. Ansari, A. Kaushik, P. R. Solanki, B. D. Malhotra, *Electroanalysis* 2009, **21**, 965-972.
- 38 R. Khan, A. Kaushik, P. R. Solanki, A. A. Ansari, M. K. Pandey, B. D. Malhotra, *Anal. Chim. Acta* 2008, **616**, 207-213.
- 39 Md. A. Ali, P. R. Solanki, M. K. Patel, H. Dhayani, V. V. Agrawal, R. John, Malhotra, B. D. *Nanoscale* 2013, **5**, 2883-2891.

### Acknowledgements

The authors thank Director NPL, New Delhi, India for the facilities. We thank Mr. Sandeep, AFM Lab, CSIR-NPL, New Delhi for the AFM analysis. Md. A. Ali and S. Srivastava are thankful to CSIR, India for the award of Senior Research Fellowships. We thank Mr. Tilak Joshi for providing facility for ITO patterning using photolithography. Authors are thankful to Dr. Venu Reddy and Prof. CheolGi Kim for the XPS measurements. V. V. A. is thankful to TSDP-DST & CSIR empower project for funding. The financial support received from Department of Science and Technology, India (Grant No. DST/TSG/ME/2008/18), the Indian Council of Medical Research, India (Grant No. ICMR/5/3/8/91/GM/2010-RHN) and to the DST Unit on Nanoscience at IIT Kanpur are gratefully acknowledged.

## Figure Captions

**Figure 1** shows an optical 3D profiling image of the ITO/glass film (a) and antTiO<sub>2</sub>-CH film on ITO coated on a glass (b). (c) 2D AFM image of antTiO<sub>2</sub> nanoparticles, inset shows the nanoparticles distribution.

**Figure 2** shows the FE-SEM images of antTiO<sub>2</sub> nanoparticles (a), antTiO<sub>2</sub>-CH/ITO film (b) and ChEt-ChOx/antTiO<sub>2</sub>-CH/ITO film.

**Figure 3**(i) Wide scan X-Ray photoelectron spectra (XPS) of various films. The XPS measurements are performed using X-ray photoelectron spectrometer (XPS, Multilab 2000, Thermo scientific) equipped with an alpha 110 hemispherical electron energy analyzer and an X-ray source. (ii) XPS spectra of the C1s region of antTiO<sub>2</sub>-CH/ITO film after deconvolution, (iii) the C1s region of ChEt-ChOx/antTiO<sub>2</sub>-CH/ITO film, (iv) N 1s core level spectra of antTiO<sub>2</sub>-CH/ITO and (v) ChEt-ChOx/antTiO<sub>2</sub>-CH/ITO films. (vi) Fourier transform infrared (FT-IR) spectrophotometer (PerkinElmer, Spectrum BX II) has been used to characterize antTiO<sub>2</sub>-CH nanocomposite and its interaction with bienzyme (ChEt-ChOx).

**Figure 4**(a) The N<sub>2</sub> adsorption and desorption isotherms of ant-TiO<sub>2</sub> nanoparticles, inset shows the pore size distribution of ant-TiO<sub>2</sub> nanoparticles and (b) Raman spectra of the ant-TiO<sub>2</sub> and antTiO<sub>2</sub>-CH films.

**Figure 5**(i) Cyclic voltammogram (CV) of (a) antTiO<sub>2</sub>-CH/ITO electrode and (b) ChEt-ChOx/antTiO<sub>2</sub>-CH/ITO bioelectrode in PBS solution (50 mM, pH 7.0, 0.9% NaCl) containing 5 mM [Fe(CN)<sub>6</sub>]<sup>3-/4-</sup> and (ii) chronoamperometric response current vs flow rate (μL/min) of (a) antTiO<sub>2</sub>-CH/ITO electrode and (b) ChEt-ChOx/antTiO<sub>2</sub>-CH/ITO bioelectrode. (iii) Electrochemical impedance spectroscopy (EIS) of (a) antTiO<sub>2</sub>-CH/ITO electrode and (b) ChEt-ChOx/antTiO<sub>2</sub>-CH/ITO bioelectrode, (inset: zoom image).

**Figure 6** (i) EIS response spectra of ChEt-ChOx/antTiO<sub>2</sub>-CH/ITO bioelectrode as a function of cholesterol oleate concentration (at flow rate of 1μL/min) attached to the inlet of microfluidic chip, (ii) EIS spectra of ChEt-ChOx/antTiO<sub>2</sub>-CH/ITO bioelectrode at different potential (0.1-0.7 V), inset: the plot between R<sub>ct2</sub> value and logarithm of potential. and (iii) the microfluidic sensor linear fit curve between EIS response and logarithm of cholesterol oleate concentration in the range of 2-500 mg/dl.

**Schematic 1** A microfluidic biochip for esterified cholesterol detection, WE= working electrode (ChEt-ChOx/antTiO<sub>2</sub>-CH/ITO), CE=counter electrode (ITO), and RE= reference electrode (Ag/AgCl) and (ii) a photograph of microfluidic biochip. (iii) Randles equivalent circuit model for EIS measurement, where  $R_s$ = solution resistance,  $R_{ct}$ = charge transfer resistance,  $Q_{dl}$ = constant phase element or double layer capacitance and  $W$ = Warburg impedance.

**Schematic 2** Functionalization of bienzyme onto antTiO<sub>2</sub>-CH surface for cholesterol detection.

**Table 1.** Pore size distribution from BET data.

Sample details	p/p <sub>0</sub>	Total pore volume (cc/g)	BET area (m <sup>2</sup> /g)	Macropore volume (cc/g)	Mesopore volume (cc/g)	Micropore volume (cc/g)	Average pore diameter (nm)
ant-TiO <sub>2</sub>	0.99707	0.2961	188.2	0.02286	0.2373317	0.0359083	6.287
antTiO <sub>2</sub> -CH	0.99940	0.1265	90.83	0.00772	0.1059716	0.0128164	5.571

**Table 2:** Sensing characteristics of cholesterol biosensor along with those reported in literature

Working electrode	Detection technique	Detection range (mg/dl)	Detection limit (mg/dl)	Sensitivity	K <sub>m</sub> Value (mg/dl)	Detection time	Ref.
Fe <sub>2</sub> O <sub>3</sub>	EIS	0.25-400	0.24	86Ω/mg dl <sup>-1</sup>	0.08	25 s	6
Chitosan-CeO <sub>2</sub>	CV	10-400	5.0	47 μA/mg dl <sup>-1</sup>	3.5	10 s	36
Chitosan-SnO <sub>2</sub>	CV	5-400	5.0	34.7 μA/mg dl <sup>-1</sup>	146.9	5 s	37
Chitosan-ZnO	CV	3-300	.....	2.0 μA/mg dl <sup>-1</sup>	8.8	15 s	38
Anatase-TiO <sub>2</sub>	CV	50-400	46.4	2.4 μA/mg dl <sup>-1</sup>	5.4	.....	26
NiO nanorods	CV	50-400	0.65	3.1 μA/mg dl <sup>-1</sup>	6.1	~ 10 s	39
Chitosan-TiO <sub>2</sub>	EIS	2-500	0.20	67.7 k Ω/mg dl <sup>-1</sup>	1.3	3s	Present Work

Figures

Figure 1

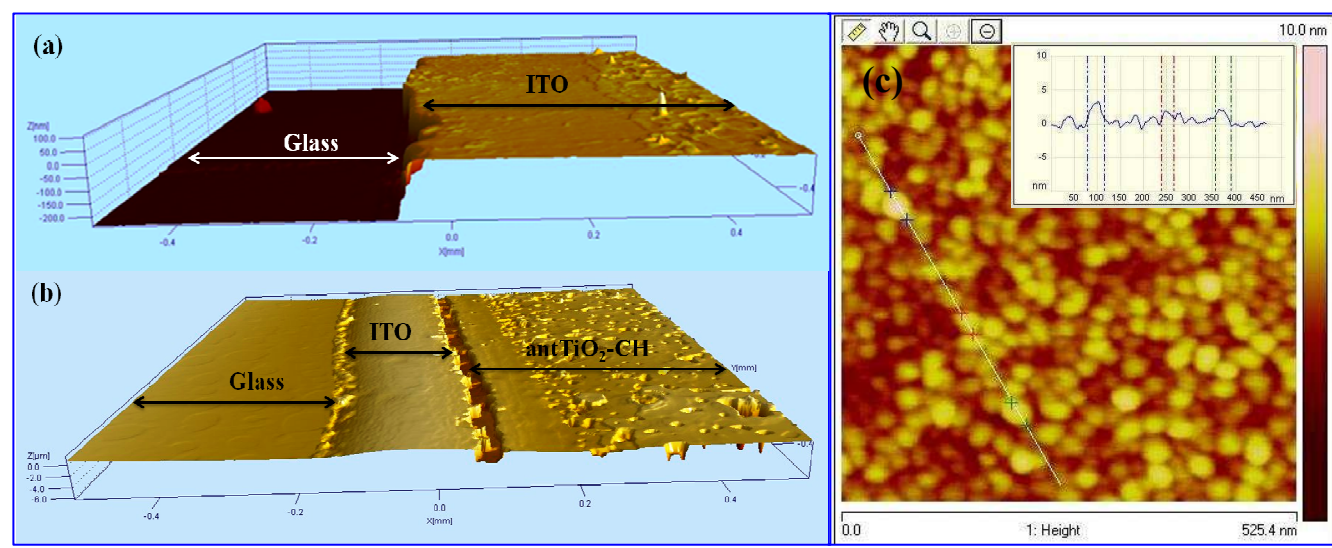


Figure 2

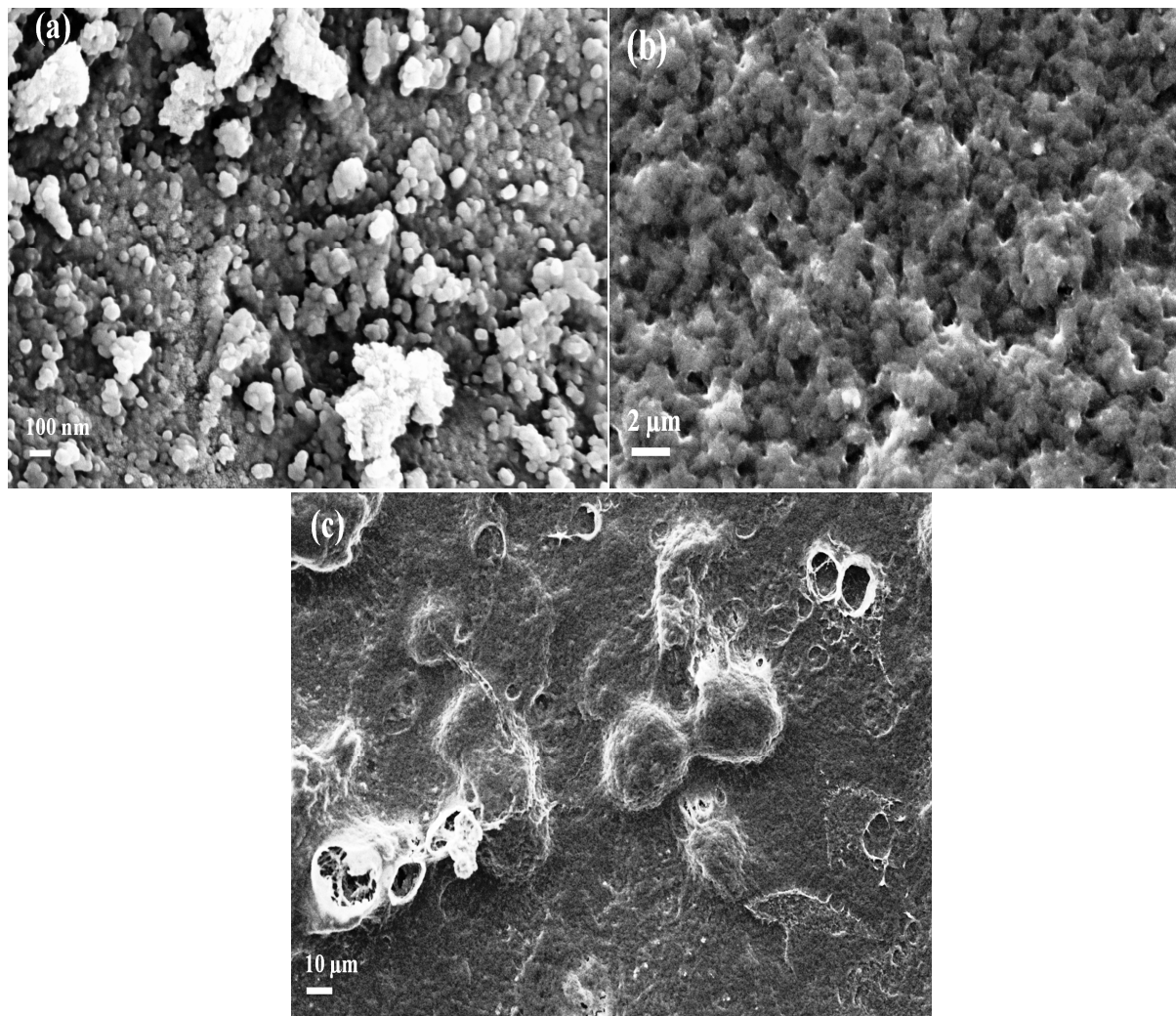


Figure 3

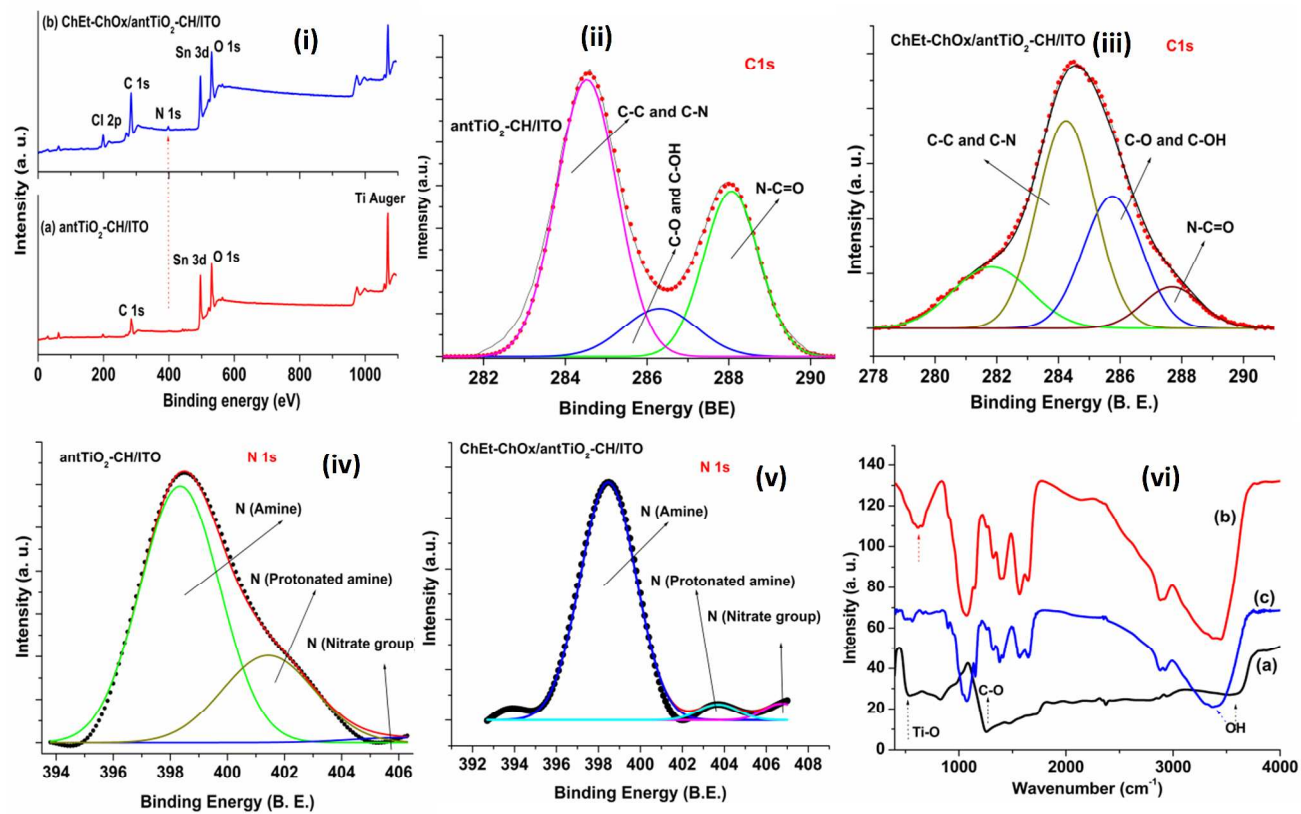


Figure 4

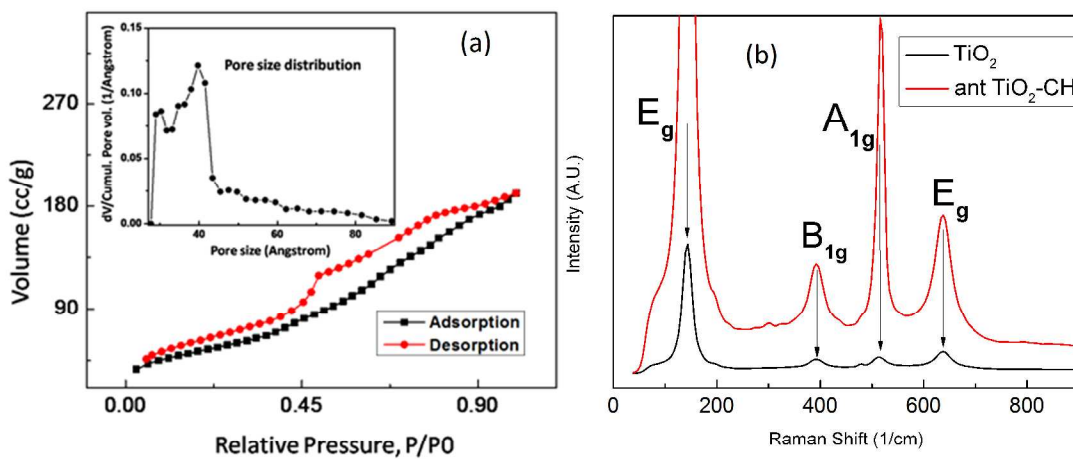


Figure 5

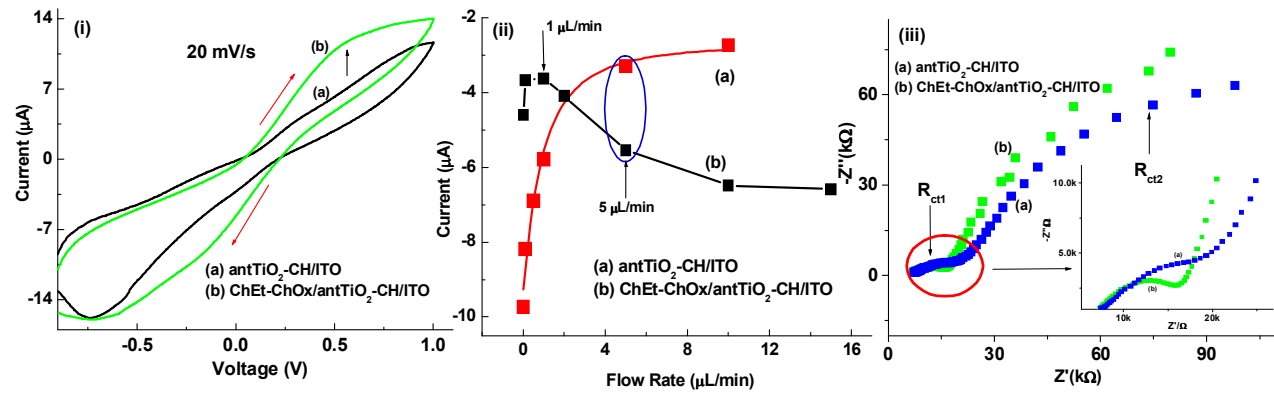
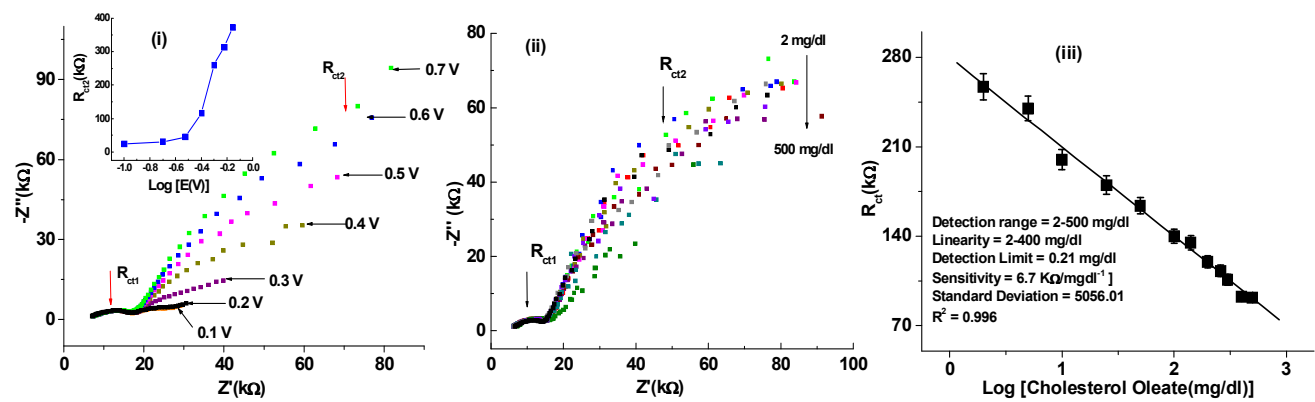
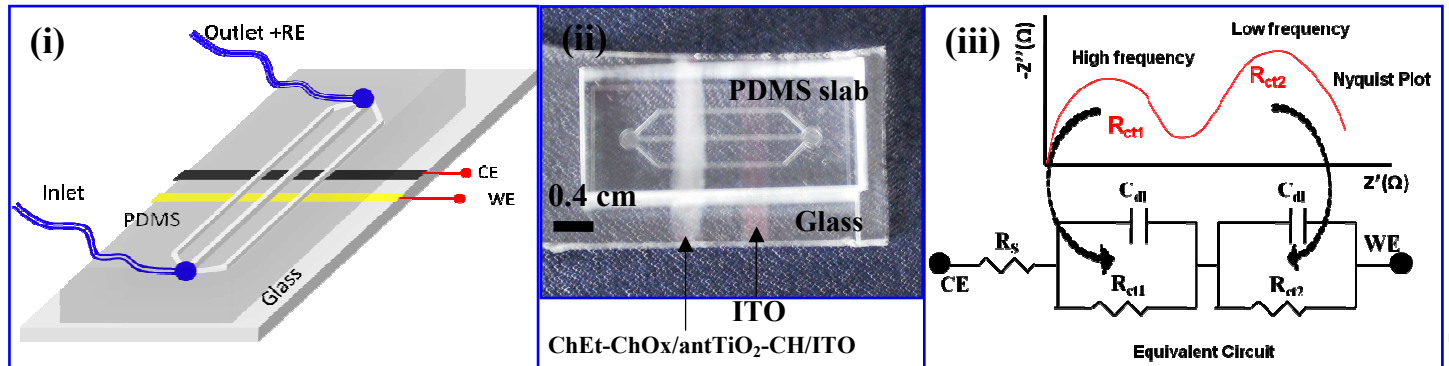


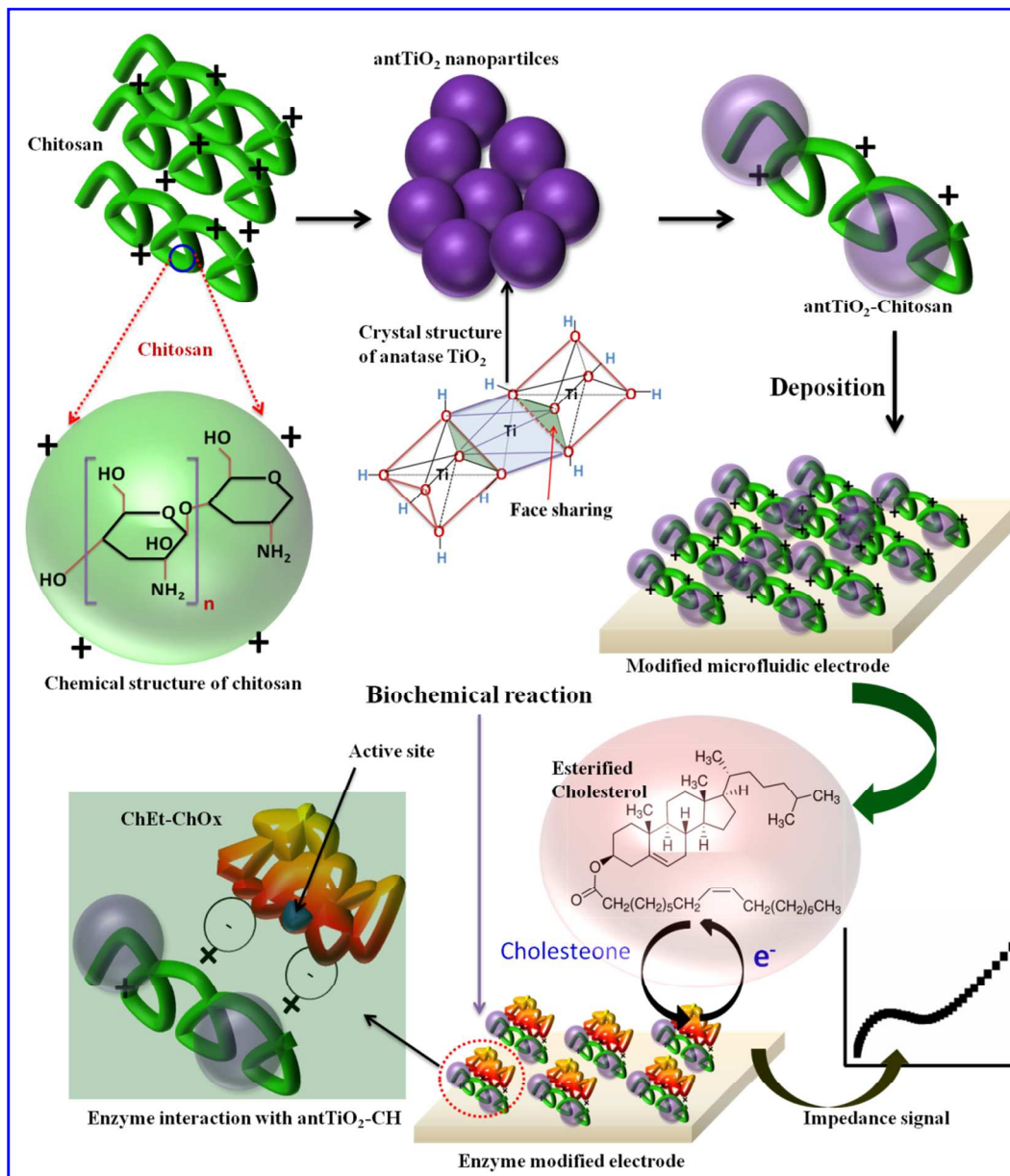
Figure 6



Schematic 1



Schematic 2



## Graphical Abstract

